applied sciences

MDPI

Article

Highway Tunnel Defect Detection Based on Mobile GPR Scanning

Junli Zhai [1], Qiang Wang [2,3,*], Haozheng Wang [2,3], Xiongyao Xie [1,2,3], Mingyi Zhou [2], Dongyang Yuan [2,3] and Weikang Zhang [2,3]

1 College of Civil Engineering, Tongji University, Shanghai 200092, China; zjl909090@tongji.edu.cn (J.Z.); xiexiongyao@tongji.edu.cn (X.X.)
2 Zhejiang Scientific Research Institute of Transport, Hangzhou 311305, China; haozheng_wang@tongji.edu.cn (H.W.); 1710197@tongji.edu.cn (M.Z.); 1832237@tongji.edu.cn (D.Y.); 1832624@tongji.edu.cn (W.Z.)
3 Key Laboratory of Road and Bridge Detection and Maintenance Technology of Zhejiang Province, Hangzhou 311305, China
* Correspondence: 18310182@tongji.edu.cn; Tel.: +86-18301963592

Abstract: In order to overcome the difficulty in rapid detection for expressway tunnels, the coherence calculation of dual-frequency radar signal in the time domain is proposed to suppress the interference. A dual-frequency (400 MHz and 900 MHz) GPR and a manipulator are developed. In the horizontal direction, it has a $-90°$~$90°$ range, a vertical rotation range from 0 to 90°, a length range from 5~9.5 m, and an antenna rotation between $-40°$~$40°$. The mobile scanning has been realized in the expressway tunnel, taking the vehicle as the mobile carrier. The research shows that: This equipment realizes the rapid detection of the tunnel without affecting the expressway's opening. The imaging algorithm recognizes the structural thickness, reinforcement distribution characteristics, and structural diseases. According to the detection carried out in Zhejiang, China, the spacing between reinforcement in the second lining is 4 cm, and the thickness of the structure is about 0.55 m. However, the reinforcement has deformed badly, and the defects are also discerned in the structure. Compared with the traditional handheld radar detection, the equipment dramatically reduces the labor demand, time, and cost and can meet engineering needs. With the proposed method, the detection time is reduced to 12 min/km from 0.5 d/km, and the cost is reduced by more than two times. Furthermore, during the detection, the traffic can be maintained normally.

Keywords: expressway tunnel; tunnel structure detection; nondestructive testing; vehicle-borne ground-penetrating radar

check for updates

Citation: Zhai, J.; Wang, Q.; Wang, H.; Xie, X.; Zhou, M.; Yuan, D.; Zhang, W. Highway Tunnel Defect Detection Based on Mobile GPR Scanning. *Appl. Sci.* **2022**, *12*, 3148. https://doi.org/10.3390/app12063148

Academic Editors: Dajun Yuan, Dalong Jin and Xiang Shen

Received: 2 March 2022
Accepted: 17 March 2022
Published: 19 March 2022

1. Introduction

With the rapid development of China's infrastructure, the expressway is essential to transportation as an important traffic artery. At present, the mileage of expressways in operation in China has exceeded 150,000 km, of which tunnels account for nearly 10%. Due to the complex and changeable engineering geological and hydrogeological conditions in the area where the expressway tunnel, coupled with the influence of the material and construction quality, the tunnel may have different degrees of tunnel leakage, lining cracking, and other defects during operation [1,2]. In order to ensure the safe operation of the expressway, it is critical to regularly detect the quality of the tunnel structure, obtain the structural information in time, evaluate the service state of the structure, and provide the data basis for formulating a maintenance plan.

As a nondestructive testing method, ground penetrating radar (GPR) can obtain the internal information of tunnel structure and figure out the hidden defects, so it has been widely used in tunnel structure detection [3–5]. However, the conventional handheld detection method has low efficiency, limited coverage area, poor working environment, and severe safety problems for the mountainous highway tunnel with long mileage. At the same time, handheld detection is easy to causes data instability in space, which increases the difficulty of radar data interpretation. Conventional detection with the high cost and low efficiency has been difficult to meet the increasing demand for tunnel mileage. With the progress of technology and the rise of all kinds of automatic equipment, tunnel detection is gradually becoming intelligent and mechanized [6,7].

Yang et al. studied the non-contact detection effect of GPR and proved the feasibility of non-contact measurement through model tests and numerical simulation [8]. Based on the non-contact detection of GPR, the research on mechanization and automation of detection has made significant progress. Zan et al. Fixed the radar antenna behind the track detection vehicle in the form of fixed support to realize the rapid acquisition of radar data [4]. Xie et al. installed GPR walking track on the shield machine to realize the circular detection of shield segments [9]. For non-contact measurement, high-frequency radar signals will form strong multiple reflected waves in the air layer, resulting in interference with the internal information of the structure [10]. Although the low-frequency radar signal has a great penetration ability, its resolution is low [11]. Alani discussed the application of different frequency radar systems in structural detection, analyzed the relationship between GPR penetration ability and frequency, and analyzed the energy weakening effect of the tunnel reinforcement layer [12]. According to the stable reflection interface of the air layer, Wang eliminated the influence of multiple reflected waves from the air layer through the background elimination method [13]. Chang eliminated the multiples with regular shape by predictive deconvolution [14].

However, the reinforcement in the tunnel structure is densely distributed, resulting in the superposition of multiple reflected waves and other signals, which increases the difficulty of data processing. At the same time, the section form of the expressway tunnel is complex and changeable. The form of fixed support or track is difficult to meet the needs of different sections. There is no track in the expressway tunnel to ensure the stability of the detection operation. Consequently, a device that can flexibly adjust the shape is necessary. In order to address the above problems and shortcomings, this paper developed a hardware system and proposed a GPR imaging algorithm.

2. Materials

2.1. System Integration

The tunnel defect detection system in this paper is called the deformable mobile detect system (DMDS). The DMDS integrates an adjustable manipulator and a dual-frequency GPR antenna. The hardware layout of the DMDS is shown in Figure 1.

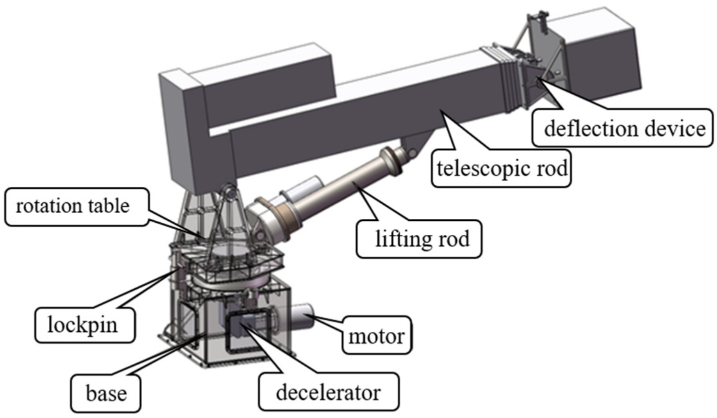

Figure 1. The DMDS has an attitude adjustment structure in different directions to adapt to the different shapes of the tunnel section.

In contrast with the regular section outline of the subway tunnel, the outline of the highway tunnel is complex and multifarious with ancillary facilities. Therefore, the manipulator must have flexible attitude adjustability. The manipulator comprises a base, rotary table, lifting rod, telescopic rod, and antenna deflection device. The manipulator can rotate within ±90° in the horizontal direction through the rotary table, rotate 0~90° in the vertical direction through the lifting rod, and expand and retract the manipulator through the telescopic rod. In order to ensure that the signal transmitted by the GPR antenna is vertically incident on the structural surface, the angle can be adjusted through the deflection facility at the top of the manipulator.

Figure 2 depicts the details of the deflection facility. The deflection facility is installed on the manipulator through the base. The deflecting is realized by the motor. In order to avoid collision during detection, a range finder is installed on one side of the bracket to monitor the distance between the antenna and the tunnel surface. The recorded distance between the antenna and the structure surface each time the signal is transmitted would be used in the subsequent data processing.

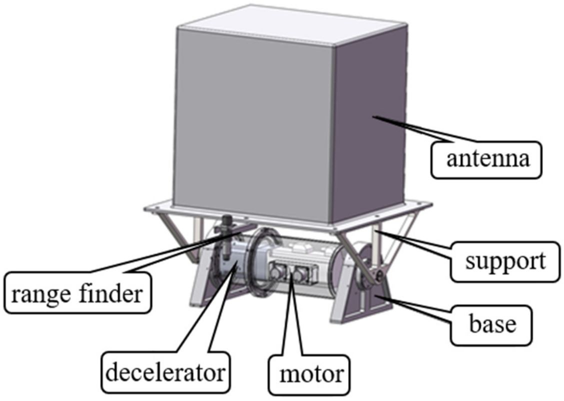

Figure 2. To ensure that the electromagnetic wave signal is incident vertically into the surface, an antenna deflection mechanism is provided on the top of the manipulator.

2.2. The GPR Antenna

The 400 MHz source pulse oscillogram had a considerable detection depth, but it could not distinguish the shallow anomalies. While the other one from 900 MHz had a shallower detection depth and higher detection precision. So in this paper, a bi-frequency GPR (see in Figure 3) that can receive 400 MHz and 900 MHz signals simultaneously is developed and manufactured to obtain the precise characteristics of the tunnel structure.

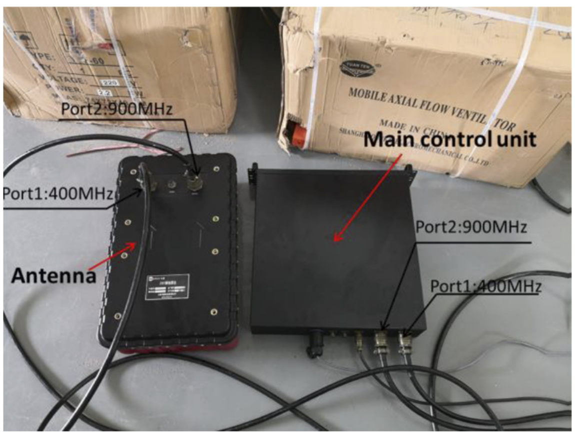

Figure 3. The GPR antenna is designed with two frequency-independent signal channels of 400 MHz and 900 MHz.

The main control unit of GPR is mainly composed of field-programmable gate array(FPGA), power management(PM), data acquisition and processing(AC&P), and radar timebase control(RTBC) unit. Upon these, the control of transmitting and receiving signals and the conversion of echo modulus is realized.

The FPGA unit adopts the XILINX SPARTAN-6 series, and the structure is based on the Virtex, a mature architecture, to realize the low risk, cost, and power consumption design. The radar data is connected with the display and control through the network port to realize the system, real-time data transmission, and display function. The PM and AC&P unit is assembled on a circuit board and placed above the substrate, responsible for the power system and processing unit.

As shown in Figure 4, the antenna is placed in the metal back cavity to enhance the antenna's penetrating ability and avoid the noise and environmental scattering signals above the ground influencing the reflected signal of the underground target, making the measured data challenging to extract. The receiving and transmitting antennas are also separated by a metal plate to improve the isolation between antennas. The top of the back cavity has a noticeable mirror effect to enhance the radiation ability of the antenna. In a specific range, the radiation pattern of the back cavity antenna with different lengths and widths is consistent. Therefore, designing the cavity size is the critical factor affecting the performance of the butterfly antenna. The size of the shielding shell should be reduced as far as possible to ensure the compactness of the radar system in the premise of enhancing the penetrating ability of the antenna.

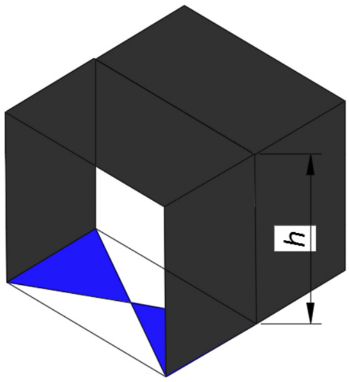

Figure 4. The antenna is placed in a metal box. The signal energy is enhanced by adjusting the height of the box.

The design of the cavity height for the mirror effect should be determined by the center frequency of the electromagnetic wave, considering that any size of the cavity is a narrowband system relative to the wide-band pulse signal. The mirror effect of the cavity top to antenna forms a two-unit antenna array, and the total intensity of downward radiation is:

$$\begin{aligned} E &= E_1\left(1 - e^{j2kh}\right) \\ k &= \frac{2\pi}{\lambda_0} \end{aligned} \tag{1}$$

where E_1 is the radiated electric field of the antenna itself; k is the wavenumber; λ_0 is the wavelength of the center frequency of the electromagnetic wave. According to the formula, we can know that when h is $1/4\ \lambda_0$, the radiated energy is the largest, two times as much as E_1.

The stability of the GPR antenna time and amplitude stability, and time-window linearity were tested before packaging. Which are defined as below:

$$\begin{aligned} J_{time} &= t_{\max} - t_{\min} \\ J_{amp} &= \frac{A_{\max} - A_{\min}}{A_{ave}} \times 100\% \\ C &= \frac{2\left|\frac{h_2-h_1}{t_2-t_1} - \frac{h_3-h_2}{t_3-t_2}\right|}{\left(\frac{h_2-h_1}{t_2-t_1} + \frac{h_3-h_2}{t_3-t_2}\right)} \end{aligned} \tag{2}$$

where J_{time}, J_{amp}, and C are the antenna's time stability, amplitude stability, and time-window linearity index, respectively. Continuously measuring the maximum and minimum arrival time of direct waves in 120 channels of radar data; h_1, h_2, h_3 and t_1, t_2, t_3 are the positions of the reflective interface at 15%, 30%, and 50% of the time window, respectively, and the corresponding arrival times of reflected waves. The test results are shown in Table 1.

Table 1. The test project results of the GPR antenna stability test.

No.	Test Item	Result
1	Time stability	0.1 ns
2	Amplitude stability	1.6%
3	Time stability of long time	0.1 ns
4	Amplitude stability of a long time	0.1 ns
5	Time-window linearity	0.9%

It is also necessary to test the independence of channels because the dual-frequency GPR needs to transmit and receive different frequencies radar signals simultaneously. One antenna is fixed during the test while the other antenna is moving. The data of the two channels is collected, and the data characteristics are observed simultaneously. Figure 5 depicts the test result. The oscillogram from the moving antenna, which is affected by the underground reinforcement, is a parabola along the moving direction. In contrast, the oscillogram from the fixed one is stable. There is no significant interference between the two signals.

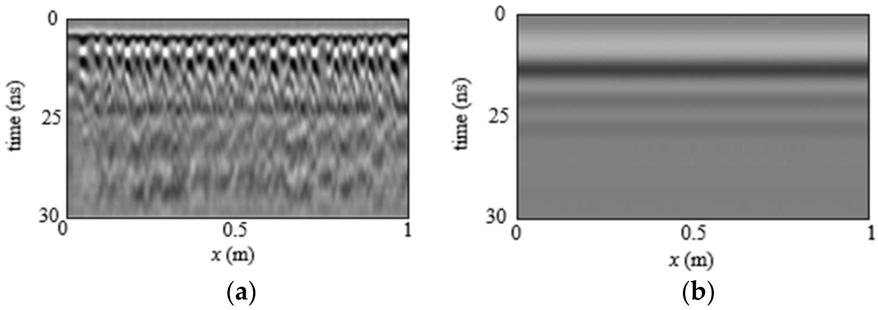

Figure 5. When only the 400 MHz antenna is moved, only changes occur in the (**a**) 400 MHz radar signal, and the (**b**) 900 MHz radar signal remains stable.

3. Methodology

The proposed bi-frequency backward projection (BBP) imaging method comprises two phases: Calculating the response amplitudes (RA) in signals and calculating the correlation between two different frequency GPR data [15].

As shown in Figure 6, the antenna moves from A-scan1 to A-scan$n$ to form a 2D radar image beneath the tunnel surface. The detection zone is divided into $n \times m$ pixels. Consequently, the position of each pixel is given by($x = i \times dx$, $z = j \times dz$)(i = 1,2,3, ... , n; mboxemphj = 1,2,3, ... , m). For the pixel in the lining, such as pixel A, the two-way travel-time (TWT) of pixel A at A-scan$k$ can be expressed as the follows:

$$t_{A,k} = \frac{2\sqrt{((i_A \times d_x) - x_k)^2 + (j_A \times d_A)^2}}{c/\sqrt{\varepsilon_1}} \tag{3}$$

The k = 1, 2, 3, ... , n is the number of A-scans; The c is the speed of electromagnetic waves propagating in a vacuum. For the pixel beneath the lining, such as pixel C, the TWT can be expressed as:

$$t_{C,k} = \frac{2\sqrt{(x_r - x_k)^2 + h^2}}{c/\sqrt{\varepsilon_1}} + \frac{2\sqrt{((i_C \times d_x) - x_r)^2 + (j_A \times d_z)^2}}{c/\sqrt{\varepsilon_2}} \tag{4}$$

where (x_r,d) is the location of the refraction point. The calculation of x_r can be realized by an approximation algorithm, as shown in Figure 7. Consequently, the response amplitude of the pixel could be obtained in the record A-scan$k$ as:

$$RA_k = \text{A-scan}k(t) \tag{5}$$

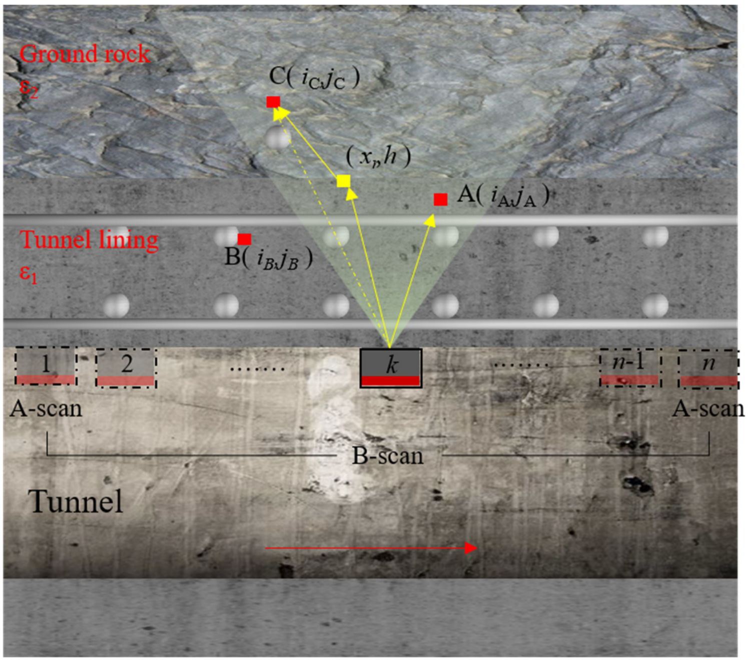

Figure 6. GPR detection process: equipment moves from A-scan1 to A-scank to acquire the information beneath the concrete segment (h is the thickness of the concrete segment, and ε is the dielectric constant).

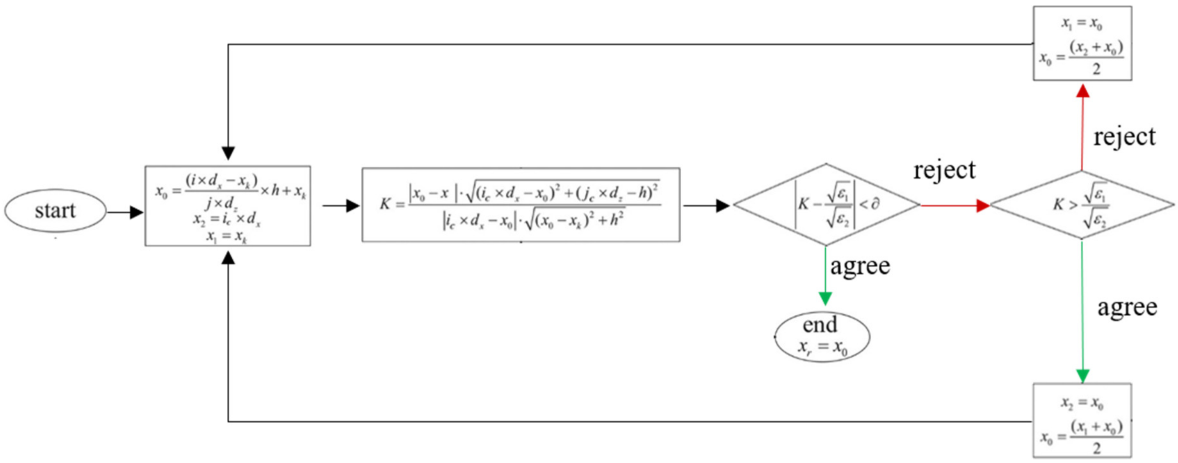

Figure 7. A successive-approximation algorithm calculates the position of the refraction point. xr is the horizontal position of the refraction point. In addition, the ∂ is a minuscule value, which defines the method's accuracy.

The response amplitude of the pixel at each A-scan can be described as two vectors as follows:

$$\begin{aligned} &R_k(400\text{ MHZ}) = \left[RA_{k,1}^{400M}, RA_{k,2}^{400M} \ldots RA_{k,n-1}^{400M}, RA_{k,n}^{400M}\right] \\ &R_k(900\text{ MHZ}) = \left[RA_{k,1}^{900M}, RA_{k,2}^{900M} \ldots RA_{k,n-1}^{900M}, RA_{k,n}^{900M}\right] \\ &k = 1, 2, \ldots i \times j \end{aligned} \tag{6}$$

The correlation between GPR profiles concerning two different frequencies will be emphasized while calculating the imaging value of pixels. The correlation between RA from B-scans concerning 400 MHz and 900 MHz dominant frequencies will be determined in this process. Specifically, the RAs from two B-scans will be multiplied as Equation (6).

$$IV_k = sum(R_k(400\text{ MHZ})\cdot R_k(900\text{ MHZ})) = \sum_{i=1}^{n} RA_{k,i}^{400M}\cdot RA_{k,i}^{900M} \quad (7)$$

Since the interference is inevitable, four kinds of radar signals are recorded in the radargram (see in Figure 8): the reflection from the target is represented by T; the noise from the background and GPR antenna is represented by N; and the diffraction and multiple-reflections are denoted by D and M, respectively. Therefore, the subsurface pixels could be classified into four types: pixels with the target (A), the pixel with diffraction (B), the pixel with multiple reflections (C), and the background. The RA of each pixel at A-scan$k$ can be described as follows:

$$RA_k = N + M + D + T \quad (8)$$

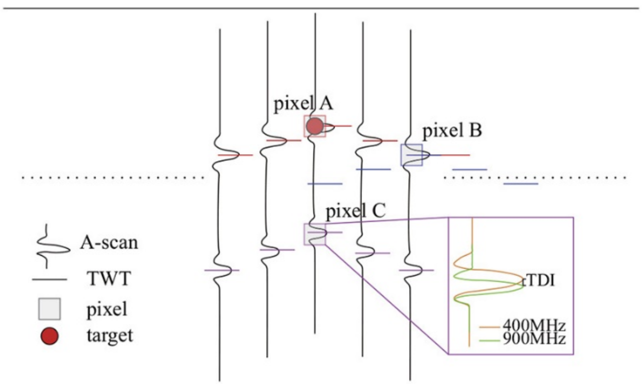

Figure 8. There is only one target at pixel A. However, the response of radar data can be found at pixel B and pixel C because of the diffraction and multiple reflections. The dashes beyond the radar signal are the TWT of pixels at each A-scan [15].

Since the signals of different kinds have little correlation, Equation (7) can be expressed as:

$$IV_k = \sum_{i=1}^{n}\left(T_{k,i}^{400M}\cdot T_{k,i}^{900M} + N_{k,i}^{400M}\cdot N_{k,i}^{900M} + D_{k,i}^{400M}\cdot D_{k,i}^{900M} + M_{k,i}^{400M}\cdot M_{k,i}^{900M}\right) \quad (9)$$

Considering that:

- For a target pixel (A), the responses would be found at each A-scan according to TWT. Furthermore, the two series of signals concerning different frequencies will maintain excellent synchronization at each A-scan. As a result, the signals from the target are strongly reinforced by the process $IV_A = \sum_{i=1}^{n} T_{A,i}^{400M}\cdot T_{A,i}^{900M}$.
- The N subjects to the Gaussian distribution and the synchronization between N^{400M} and N^{900M} is quite weak because of their randomness. Therefore, the IV of background represented by $IV_k = \sum_{i=1}^{n} N_{k,i}^{400M}\cdot N_{k,i}^{900M}$ could be ignored.
- The blue dashes in the picture represent the TWT of pixel B (the pixel with diffraction) at each A-scan. According to the TWT, only one response could be observed at all A-scans. It means D_B = [0,0,..,D,0,..,0]. Consequently, the IV of the pixels diffraction $IV_B = \sum_{i=1}^{n} D_{B,i}^{400M}\cdot D_{B,i}^{900M}$ is a small value compared to IV_A.
- The synchronization between M^{400M} and M^{900M} sharply decreases because of the time delay inequality (TDI) between multiple reflections concerning different frequencies.

Consequently, the IV of pixels with multiple reflections $IV_C = \sum_{i=1}^{n} M_{C,i}^{400M} \cdot M_{C,i}^{900M}$ should be less than IV_A.

As a result, the interference due to noise, multiple reflections, and diffraction could be eliminated with this innovative methodology.

4. Experiment and Results

4.1. Data Acquisition

The experiment was conducted in a highway tunnel in Zhejiang, China. This tunnel has been operating safely for about 10 years. The structure of the tunnel is supported by reinforcement and concrete. First, the DMDS was installed on the vehicle. Then, the manipulator's attitude was adjusted to meet the section shape of the tunnel. Finally, the vehicle moved forward, and the GPR scanning was conducted.

In order to obtain accurate coordinate information, GPS is used for positioning at the beginning of detection. The obtained positioning information corresponds to the mileage of the design to obtain the mileage at the starting point of the detection line. However, the GPS signal is weak in the tunnel. Consequently, the encoder recorded the driving distance and converted it into the mileage in the tunnel.

The scanning of the GPR profile was 30 km/h. The distance between two adjacent A-scans was 2 cm, and there were 1024 sample points in an A-scan. The time window of scanning was about 50 ns. Consequently, the time distance between every sample point was 0.05 ns. The operation of the RMMS, including attitude adjusting and scanning, took about 10 min to complete. In the end, 1 km GPR profiles with two different frequencies were obtained. The efficiency of the DMDS was significantly higher than that of the traditional detection method, even disregarding the safety guarantee during conducting. Figure 9 depicts the data acquisition process by the DMDS.

Figure 9. When the manipulator is adjusted to a reasonable attitude, start the vehicle to carry out a quick scan along the measurement line.

Considering the amount of data, this paper selects a 10 m scale profile (from mileage ZK39 + 752 to 762) in the obtained GPR data for discussion. Figure 10 depicts the preprocessed GPR data with 400 MHz and 900 MHz. After direct wave interception, gain, and background elimination, the horizontal multiple reflection waves caused by the air layer are filtered out. Still, a small amount of interference caused by the reinforcement layer and disease remains, especially in the 900 MHz signal. The undulating reflective interface caused by the reinforcement layer is visible around 10 ns. However, the reflection interface is continuous due to scattered waves. Consequently, the spacing of the reinforcement is difficult to determine. Furthermore, apparent abnormalities can be seen in the range from ZK39 + 754 to +760, presumed to be structure diseases. Since the interference of shallow information masks the adequate deep information, it is difficult to obtain the bottom information of the thickness of the second-lined structural layer.

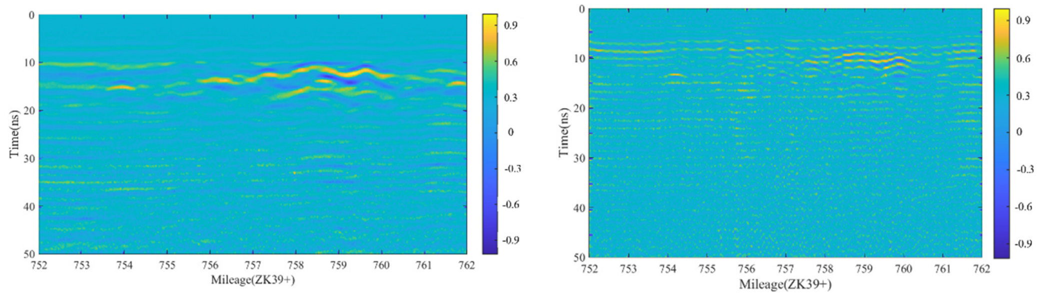

(**a**) (**b**)

Figure 10. Radar images after preprocess show a distinct layer of rebar reflections, but the reinforcement is not recognizable. Moreover, due to the multiple reflected wave interference caused by the deformed high reinforcement layer, the thickness of the second-lined structure cannot be identified. (**a**) 400 MHz; (**b**) 900 MHz.

4.2. Imaging Result and Analysis

In order to obtain the detection results such as rebar spacing, second-lining thickness, and disease characteristics, the detection area is imaged by the BBP algorithm. The imaging result is shown in Figure 11.

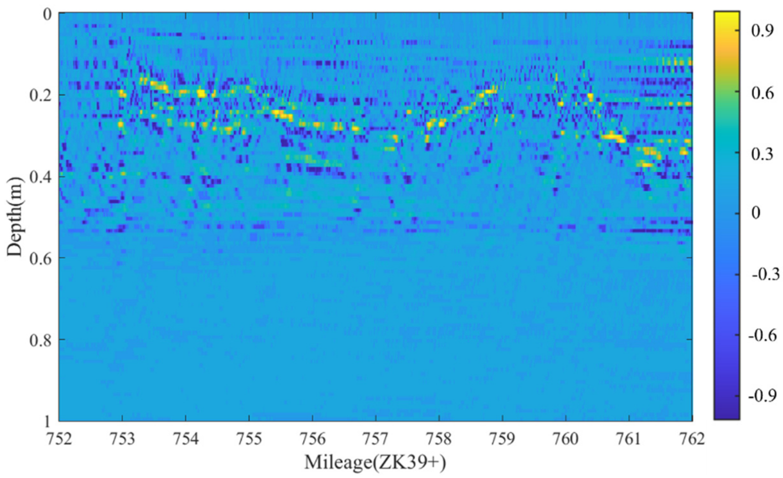

Figure 11. With the BBP algorithm, the position of the reinforcement, the thickness of the structural layer, and the deformation of the reinforcement layer are clearer in the image.

Within the range of ZK39 + 753~755, the double-layered dot-like reflective energy concentration is visible, and the depth of these concentrations fluctuates slightly at about 0.25 m. The horizontal direction is evenly distributed in a 4 cm spacing. Consequently, it is presumed to be a double-layered reinforced skeleton inside the structure. After ZK39 + 755, the reflected energy is significantly weakened, and the reflection interface is deformed. Therefore the moisture content at this location is inferred to be relatively high, resulting in rapid attenuation of electromagnetic signals. The upper reflective layer disappears at ZK39 + 757 and 759. Consequently, it is speculated that the seepage channel is developed there. In the range from ZK39 + 758 to 760, the steel layer can be seriously deformed and protrude into the tunnel. It is inferred that there is a defect in the structure. An obvious sub-interface can be seen at a depth of about 0.55 m, which should be the tunnel second lining and primary lining sub-interface.

Based on the above analysis, it can be seen that the spacing of the reinforcement in the structure is about 4 cm, and the thickness of the second-lined structure is about 0.55 m, which is consistent with the design. The defects of the tunnel structure are mainly distributed in ZK39 + 755 and ZK39 + 758~760. After the inspection was completed, the corresponding location of the tunnel was inspected for visual quality, and obvious cracks and groundwater seepage (repaired) were visible near ZK39+760, as shown in Figure 12.

Figure 12. Structural defects are visible at the corresponding anomalous locations in the GPR profile.

5. Discussion

The defect in the tunnel structure is a key factor affecting the safe operation of the tunnel. Consequently, the regular inspection of the tunnel structure is essential for engineers. GPR has been widely used in structural health testing as the main nondestructive testing method. Engineers scan the tunnel structure by riding a lift truck with a handheld radar antenna (as shown in Figure 13a). It is evitable to interrupt the traffic and close the road for safety. This manual detection method is inefficient, and there are also potential safety hazards in the operation of climbing vehicles. For a 1 km long tunnel, the manual inspection method usually requires 4~5 experienced inspectors, and the operation would take 12–24 h.

(**a**) (**b**)

Figure 13. (**a**)Traditional testing methods require inspectors to work on ascending equipment; (**b**) In the proposed method the inspector can stay in the vehicle to conduct the detection.

In order to improve the efficiency of defect detection, the DMDS is developed in this paper. The field experiment has been carried out to verify the ability to figure out the defects in the tunnel structure. The overall detection process takes only about 15 min for a 3 km long tunnel with a driver and an operator. Furthermore, the operator could stay in the vehicle during the detection (shown in Figure 13b). Safety is guaranteed, and the traffic does not have to be interrupted.

Table 2 shows the comparison between the proposed DMDS and the traditional detection method. The method proposed in this paper has significant efficiency, labor, cost, and safety optimization effects compared with traditional methods.

Table 2. Comparison of benefits.

Item	Traditional	Proposed Method
efficiency	0.5 d/km	12 min/km
Impact on traffic	Close the road	No impact
Cost	30,000~40,000 Yuan/km	<10,000 Yuan/km
Safety	Fall risk and traffic risk	Safe

The method mentioned in this paper is mainly used for the rapid detection of highway tunnels. The detection speed can reach up to 50 km/h according to the radar sampling frequency. However, for safety reasons, it is recommended to control the detection speed within 30 km/h. Due to the rapid detection work moving speed, and there are more auxiliary facilities in the tunnel, before the implementation of the detection work should be based on the tunnel section design drawings of the layout of the measurement line for the reasonable arrangement to avoid the occurrence of antenna collision accidents. How to quickly avoid obstacles in high-speed driving conditions and the protection of radar antennas during detection are the key research directions in the future. Furthermore, it is imperative to use the method of machine learning instead of manual identification of diseases and obtain the quantitative parameters of defects. A sufficient number of sample sets is the basis of machine learning methods. In the future, we will achieve this goal through the proposed GPR fast detection method.

6. Conclusions

This paper firstly develops the hardware system of the tunnel inspection vehicle and studies the hardware parameter selection and parameter calculation method of the image fast acquisition system. Then, images of cracks in the tunnel lining are analyzed, and practical tests are carried out at the tunnel site. Finally, a comparison is also made with pure detection. The main conclusions are as follows:

(1) The device has horizontal rotation, vertical rotation, length expansion, and antenna angle rotation functions. In the horizontal direction, it has a $-90°$~$90°$ range, a vertical rotation range from 0 to $90°$, a length range from 5~9.5 m, and an antenna rotation between $-40°$~$40°$. It can be applied to detect tunnels with different section shapes combined with mobile vehicles.

(2) Reflections and multiple reflections in the air between the surface of the tunnel structure and the antenna can cause serious interference. The shaking of the vehicle as it moves forward can also cause disturbances. Recording the distance change during the scan with a rangefinder eliminates interference due to shaking. Regular multiple ripples can be removed through gain, filtering, and background elimination. The BBP algorithm can suppress interference caused by deformed steel skeletons and defects.

(3) Through the method proposed in this paper, quantitative parameters such as the spacing of the reinforcement bars, the thickness of the second lining, and the location of the disease in the tunnel structure can be obtained.

(4) The method proposed in this paper improves the working environment of highway tunnel structure detection, improves the operation speed, reduces the risk in operation, and has considerable economic benefits compared with traditional methods.

Author Contributions: Conceptualization, Q.W. and X.X.; methodology, H.W.; software, M.Z.; validation, J.Z. and H.W.; resources, J.Z.; data curation, D.Y. and W.Z.; writing—original draft preparation, J.Z.; writing—review and editing, Q.W. All authors have read and agreed to the published version of the manuscript.

Funding: This research was funded by the National Key R&D Program of China under grants 2019YFC0605100, 2019YFC0605103, National Nature Science Funds of China under grants 52038008, 42107216 and 4210071391, the Key Science and Technology Projects in Transportation Industry by Ministry of Transport of the People's Republic of China in 2021(Grant No. 2021-MS2-061), the Project of Science and Technology Program of Department of Transport (Grant No.2021014) and the Independent Scientific Research Project of Zhejiang Scientific Research Institute of Transport (Grant No. ZK202205 and ZK202206).

Institutional Review Board Statement: Not applicable.

Informed Consent Statement: Not applicable.

Data Availability Statement: Not applicable.

Acknowledgments: Thanks to the Bureau of Transportation of Lishui for providing the tunnels for detection.

Conflicts of Interest: The authors declare no conflict of interest.

References

1. Xu, Y.; Li, D.; Xie, Q.; Wu, Q.; Wang, J. Automatic defect detection and segmentation of tunnel surface using modified Mask R-CNN. *Measurement* **2021**, *178*, 109316. [CrossRef]
2. Ye, F.; Qin, N.; Liang, X.; Ouyang, A.; Qin, Z.; Su, E. Analyses of the defects in highway tunnels in China. *Tunn. Undergr. Space Technol.* **2021**, *107*, 103658. [CrossRef]
3. Qin, H.; Zhang, D.; Tang, Y.; Wang, Y. Automatic recognition of tunnel lining elements from GPR images using deep convolutional networks with data augmentation. *Autom. Constr.* **2021**, *130*, 103830. [CrossRef]
4. Zan, Y.; Li, Z.; Su, G.; Zhang, X. An innovative vehicle-mounted GPR technique for fast and efficient monitoring of tunnel lining structural conditions. *Case Stud. Nondestruct. Test. Eval.* **2016**, *6*, 63–69. [CrossRef]
5. Feng, D.; Wang, X.; Zhang, B. Specific evaluation of tunnel lining multi-defects by all-refined GPR simulation method using hybrid algorithm of FETD and FDTD. *Constr. Build. Mater.* **2018**, *185*, 220–229. [CrossRef]
6. Negri, S.P.; Basile, V.; Valori, M.; Gambino, B.; Fassi, I.; Tosatti, L.M. A modular mobile robotic architecture for defects detection and repair in narrow tunnels of CFRP aeronautic components. *Robot. Comput.-Integr. Manuf.* **2019**, *55*, 109–128. [CrossRef]
7. Menendez, E.; Victores, J.G.; Montero, R.; Martínez, S.; Balaguer, C. Tunnel structural inspection and assessment using an autonomous robotic system. *Autom. Constr.* **2018**, *87*, 117–126. [CrossRef]
8. Yang, Y.Q.; He, S.H.; Qi, F.L.; Jiang, B. Simulation test of GPR non-contact defection on lining of railway tunnel. *Chin. J. Rock Mech. Eng.* **2011**, *30*, 1761–1768. (In Chinese)
9. Zeng, L.; Zhou, B.; Xie, X.; Zhao, Y.; Liu, H.; Zhang, Y.; Shahrour, I. A novel real-time monitoring system for the measurement of the annular grout thickness during simultaneous backfill grouting. *Tunn. Undergr. Space Technol.* **2020**, *105*, 103567. [CrossRef]
10. Johnston, B.; Ruffell, A.; McKinley, J.; Warke, P. Detecting voids within a historical building façade: A comparative study of three high frequency GPR antenna. *J. Cult. Herit.* **2018**, *32*, 117–223. [CrossRef]
11. Gennarelli, G.; Catapano, I.; Ludeno, G.; Noviello, C.; Papa, C.; Pica, G.; Soldovieri, F.; Alberti, G. A low frequency airborne GPR system for wide area geophysical surveys: The case study of Morocco Desert. *Remote Sens. Environ.* **2019**, *223*, 111409. [CrossRef]
12. Alani, A.M.; Tosti, F. GPR applications in structural detailing of a major tunnel using different frequency antenna systems. *Constr. Build. Mater.* **2018**, *158*, 1111–1122. [CrossRef]
13. Wang, Y. *Study on Ground-Penetrating Radar Multiple Waves Identification and Suppression Method*; China University of Geosciences: Beijing, China, 2017.
14. Chang, Y.-F.; Ma, Y.; Lin, C.-M.; Lee, J.-H. Reverberation reduction in ultrasonic images via predictive deconvolution. *NDT&E Int.* **2008**, *41*, 235–241.
15. Xie, X.; Zhai, J.; Zhou, B. Back-fill grouting quality evaluation of the shield tunnel using ground penetrating radar with bi-frequency back projection method. *Autom. Constr.* **2021**, *121*, 103435. [CrossRef]